

Cite this article as: Qi Yuxuan, Mao Liang, Li Peiyong, et al. Dynamic Behavior, Energetic Characteristics, and Failure Mechanism of High-Density W-Zr-Ti Reactive Alloy[J]. Rare Metal Materials and Engineering, 2025, 54(07): 1687-1696. DOI: <https://doi.org/10.12442/j.issn.1002-185X.20240338>.

ARTICLE

# Dynamic Behavior, Energetic Characteristics, and Failure Mechanism of High-Density W-Zr-Ti Reactive Alloy

Qi Yuxuan<sup>1</sup>, Mao Liang<sup>1</sup>, Li Peiyong<sup>1</sup>, Liu Guitao<sup>2</sup>, Tian Longnian<sup>1</sup>, Jiang Chunlan<sup>1</sup>

<sup>1</sup> State Key Laboratory of Explosion Science and Safety Protection, Beijing Institute of Technology, Beijing 100081, China; <sup>2</sup> Ningbo Branch of Chinese Academy of Ordnance Science, Ningbo 315103, China

**Abstract:** A high-density tungsten-zirconium-titanium (W-Zr-Ti) reactive alloy was prepared by powder metallurgy. This alloy exhibits high density, high strength, and violent energy release characteristics, resulting in outstanding penetration and ignition abilities. Dynamic impact experiment demonstrated its strain rate hardening effect, and the energetic characteristics were investigated by digital image processing technique and thermal analysis experiment. The results show that W-Zr-Ti reactive alloy performs compressive strength of 2.25 GPa at 5784 s<sup>-1</sup> strain rate, and its exothermic reaction occurs at about 961 K. Based on the explosion test and shock wave theory, thresholds of enhanced damage effect are less than 35.77 GPa and 5.18×10<sup>4</sup> kJ/m<sup>2</sup> for shock pressure and energy, respectively. Furthermore, the transformation of fracture behavior and failure mechanism is revealed, which causes the increase in compressive strength and reaction intensity under dynamic loading.

**Key words:** reactive alloy; dynamic behavior; energetic characteristics; failure mechanism

## 1 Introduction

Tungsten (W) alloy is one of the most commonly used materials in impact engineering. As a typical fragment and penetrator material, it possesses high density and good mechanical properties<sup>[1-2]</sup>, leading to a superior damage ability during penetration<sup>[3]</sup>. Although W alloy is suitable for the structural design due to its properties and cost, mushrooming process results in a poorer penetration performance compared with depleted uranium alloy. Meanwhile, W alloy remains inert in the condition of impact<sup>[4]</sup>, which restricts its damage capability behind the protection of armor. Therefore, it is necessary to develop a new kind of W alloy with self-sharpening or energy release behavior. Previously, comprehensive works and efforts have been made in the advanced W alloy design<sup>[5-7]</sup>, mechanical properties<sup>[8-9]</sup>, characteristics prediction<sup>[10-11]</sup>, and engineering applications<sup>[12-14]</sup>.

Based on the practical purposes, previous research may be divided into two categories. One is aimed to improve the penetration capability by exploring mechanical properties or

generating self-sharpening behavior. Significant works<sup>[15-17]</sup> reported that high-entropy W alloys exhibit excellent mechanism properties and high susceptibility to adiabatic shear banding. Especially, brilliant self-sharpening behavior occurs, when rhombohedral  $\mu$  phase is introduced into face-center cubic (fcc) matrix<sup>[15]</sup>. W-fiber with Zr-based metallic glass matrix materials have the similar self-sharpening behavior as well<sup>[18]</sup>. The other is introducing energetic element into alloy system, which can stimulate violent combustion and enhance damage effect behind the armors<sup>[19]</sup>. Combustion experiments demonstrated that debris generated from penetrator could be initiated by adding Zr<sup>[20]</sup>, even W could participate in the chemical reaction under explosion loading<sup>[21]</sup>. Hence, tungsten-zirconium (W-Zr) alloy becomes a typical energetic structural material<sup>[22]</sup> with high strength and energy level<sup>[23-24]</sup>. Further research<sup>[25-26]</sup> found that effective energy and impact pressure give contributions to the energy release of reactive alloy fragments. However, the applications of W-Zr reactive alloy are still restricted by the contradiction between detonation driven resistance and impact ignition reliability.

Received date: June 04, 2024

Foundation item: National Natural Science Foundation of China (12002045); Supported by State Key Laboratory of Explosion Science and Safety Protection, Beijing Institute of Technology (QNK22-09)

Corresponding author: Jiang Chunlan, Ph.D., Professor, State Key Laboratory of Explosion Science and Safety Protection, Beijing Institute of Technology, Beijing 100081, P. R. China, Tel: 0086-10-689127581, E-mail: [jiangchunwh@bit.edu.cn](mailto:jiangchunwh@bit.edu.cn)

Copyright © 2025, Northwest Institute for Nonferrous Metal Research. Published by Science Press. All rights reserved.

Moreover, the balance between penetration behavior and energy release is essential to come into consideration as well. Therefore, fragment coating<sup>[27]</sup> and element addition<sup>[28]</sup> were adopted recently. It is found that element Ti would enhance strength and ductility of reactive alloy, resulting in damage potential preservation and brilliant ballistic performance<sup>[29]</sup>. Zr-Ti phase diagram reveals that Ti would reduce transition temperature simultaneously.

Hence, high-density tungsten-zirconium-titanium (W-Zr-Ti) reactive alloy with brilliant penetration and ignition abilities was proposed. Furthermore, quasi-static compression, dynamic impact, thermal analysis, and explosion test were conducted to reveal its dynamic behavior, energetic characteristics, and failure mechanism. In addition, shock pressure and energy, kinetics parameters, and constitutive model have been calculated for the future research. This research provides some meaningful results and analyses on this new kind of reactive alloy for engineering applications.

## 2 Experiment

High-density W-Zr-Ti reactive alloy with the mass ratio of W:Zr:Ti=70:15:15 and the density of 10.43 g/cm<sup>3</sup> was prepared by powder metallurgy in this research. Fig. 1a illustrates the process of alloy preparation. Firstly, raw metal powders were mixed in the atmosphere of inert gas, and then polymer binder was added into the mixture for pelleting. Afterwards, vacuum sintering furnace was employed for dry degreasing at 873 K and sintering at 1573 K, which reinforced the interaction between metal powders and strengthened the reactive alloy. Finally, the alloy blank stood in the air for residual stress relaxation, and was machined into experimental samples, as shown in Fig. 1b. The sizes of samples were  $\Phi 9$  mm $\times 9$  mm,  $\Phi 5$  mm $\times 3$  mm, and  $\Phi 6.5$  mm $\times 6.5$  mm for quasi-static compression, dynamic impact, and explosion test, respectively.

In order to understand the microstructure of the reactive alloy and reveal its failure mechanism in various loading conditions, field emission scanning electron microscope (SEM, FEI Quanta 650 FEG) operated at the voltage of 20 kV and equipped with energy dispersive spectrometer (EDS, Oxford X-MAX) was employed for microstructure observation and element analysis. Further refined research was conducted using field emission transmission electron microscope (TEM, FEI Technai G2 F30) operated at the voltage of 200 kV. TEM sample was fabricated by the method of ion-beam thinning. For the observation of phase distribution and interaction information in details, high-angle annular dark field (HAADF) and high-resolution transmission electron microscope (HRTEM) images were acquired simultaneously. Selected area electron diffraction (SAED) patterns were calibrated to clarify the crystal structure of phases in the reactive alloy.

In this study, mechanical and energetic properties of the reactive alloy under the quasi-static compression, dynamic and explosive loading were investigated. MTS810 hydraulic universal testing machine manufactured by American MTS company was used to conduct the quasi-static compression

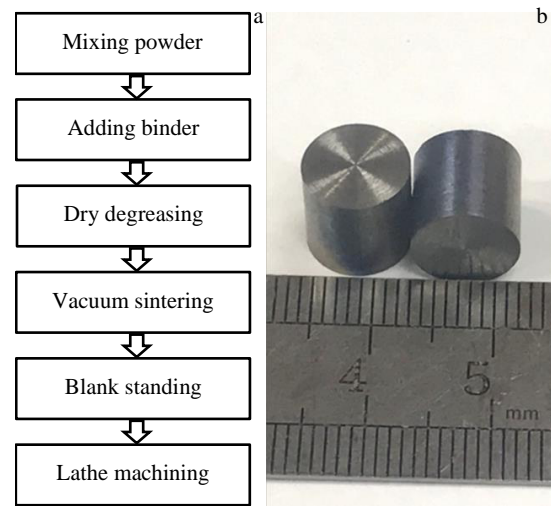


Fig.1 Process diagram (a) and experimental samples (b) of reactive alloy

test. Loading strain rate and sampling frequency were set as 0.001 s<sup>-1</sup> and 5.0 Hz, respectively. For the reliability of compressive data, three times tests were conducted. Fig. 2 illustrates schematic diagram of split Hopkinson pressure bar (SHPB) test system. Striker bar was launched by the high-pressure gas in the barrel, which impacted the incident bar and formed an initial stress wave pulse. This pulse propagated from incident bar to the sample, and then entered into transmitted bar. Residual energy of the pulse was dissipated by absorption bar and damper. During the test, stress wave pulse was handled and filtered by the wave shaper. Sleeves and spacers were employed to protect the test bars. Chemical reaction phenomenon was recorded by high-speed camera. The pulse data was recorded by strain gauge and data-processing system. By adjusting the gas pressure, incident bar velocity was controlled for different loading strain rate. Stress-strain curves at different strain rates were calculated by the reflective and transmitted pulses, as follows:

$$\sigma = \frac{A_b E_b}{A_0} \varepsilon_t \quad (1)$$

$$\varepsilon = -\frac{2c_0}{l_0} \int_0^t \varepsilon_r d\tau \quad (2)$$

$$\dot{\varepsilon} = -\frac{2c_0}{l_0} \varepsilon_r \quad (3)$$

where  $\sigma$ ,  $\varepsilon$ , and  $\dot{\varepsilon}$  refer to the stress, strain, and strain rate of the material, respectively;  $t$  means the calculated time;  $A_0$  and  $l_0$  are the cross-sectional area and length of the sample, respectively;  $A_b$ ,  $E_b$ , and  $c_0$  represent the cross-sectional area, elastic modulus, and elastic wave speed of the bar, respectively;  $\varepsilon_r$  and  $\varepsilon_t$  are the strain in the transmitted and incident bar measured in the experiment, respectively.

Differential scanning calorimetry thermo-gravimetry (DSC/TG, NETZSCH STA 449 F3) were performed for further investigation. Reactive alloy samples were tested in the air atmosphere with heating rates of 5, 10, and 20 K/min. Before the heating loading, reactive alloy samples were polished by

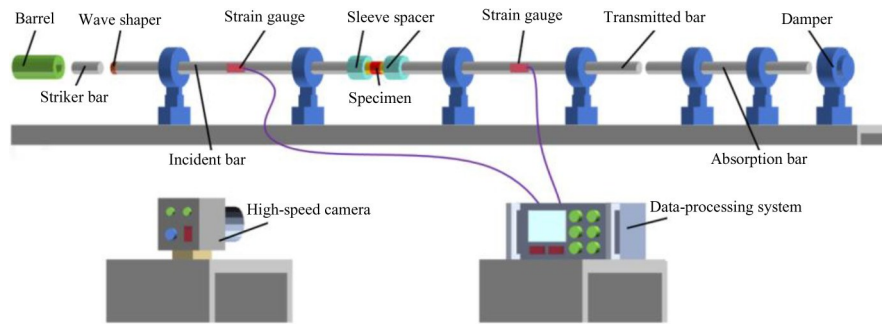


Fig.2 Schematic diagram of SHPB test system

sandpaper, refraining from the obstruction of the oxidation layer caused by wire-electrode cutting process. Moreover, reaction kinetics parameters in Arrhenius equation were estimated during the energy released process.

Reactive fragments have to suffer explosion loading and keep their damage potential until arriving the targets. It is necessary to conduct explosion test in order to verify its availability in the fragment structure and reveal its comprehensive damage effect. We conducted a fragment structure equipped with high-density W-Zr-Ti reactive alloy fragments. The reactive fragments were prefabricated surrounding the charge made of JH-14 explosive. Booster and detonator were installed in the center of structure charge to ensure the sufficient explosion and uniform fragment loading condition. Fan-shaped target made of 6 mm Q235 steel was installed at a distance of 10 m far from the structure, as shown in Fig. 3a. Behind the fan-shaped target, six 10 L fuel tanks filled with 5 L aviation kerosene were put on the bracket, as shown in Fig. 3b. The velocity of reactive fragment was measured by velocity detection targets coordinated with multiple channel recorder, as shown in Fig. 3c. For the safety of staff and equipment, a concrete wall was built as shelter. After the explosion, the damage effect of fuel tanks and fragment velocity were recorded.

### 3 Results and Discussion

#### 3.1 Microstructure characteristics

Fig. 4 presents microstructure observation of the reactive alloy. It is found that the reactive alloy is composed of large-sized spheres and small-sized particles. Element W is mainly distributed in the small-sized particles, while elements Zr and Ti exist in the large-sized spheres. Moreover, elements Zr and Ti infiltrate into the gap of W particles and form the bonded matrix, corresponding to the dispersive spots outside the large-sized spheres, as shown in Fig. 4a–4d. It is estimated that the Zr-Ti solid solution remains hexagonal close-packed (hcp) structure, because the spheres maintain their profile without melting during the powder metallurgy.

To further clarify the microstructure of bonded matrix and its interface characteristic with the reinforced particles, TEM microscopic observation and analysis were conducted. TEM images and SAED patterns of the reactive alloy are shown in Fig. 4e–4h. HAADF-STEM image illustrates that reinforced

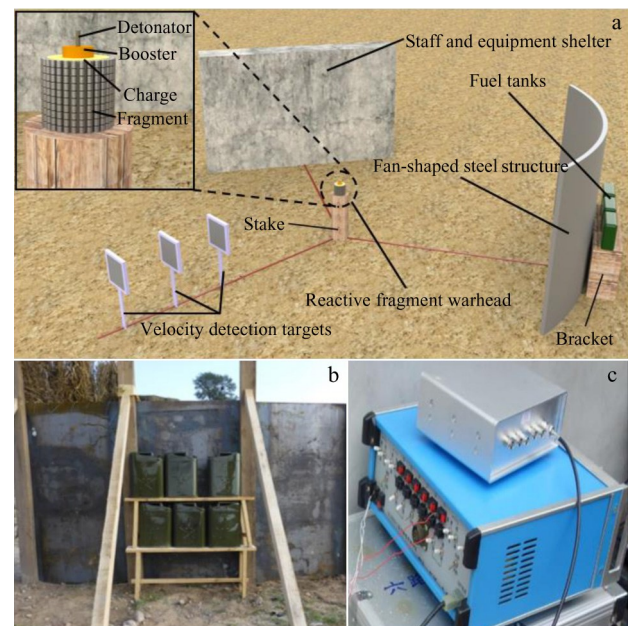


Fig.3 Schematic diagram of experiment (a); photographs of fuel tanks (b) and channel recorder (c)

particles are in the range of 0.5–2.5  $\mu\text{m}$ . These particles are embedded in the bonded matrix, and some of them contact with each other, as shown in Fig. 4e. In this case, force chains and networks might be generated among these particles, playing an important rule in the improvement of the compressive strength. Meanwhile, bonded matrix material performs fine dispersion during the sintering, resulting in quality interface with the reinforced particles, as shown in Fig. 4f.

Fig. 4g and Fig. 4h present SAED patterns of bonded matrix and reinforced particles, respectively. It is illustrated that all the matrix and particles have body-centered cubic (bcc) structure. Hence, lattice constants of the matrix and particles are 0.3448 and 0.3158 nm, respectively, which provides further evidence that the matrix consists of Zr-Ti solid solution and the particles are composed of element W. The addition of Ti content reduces the lattice constant of pure Zr matrix. There is a small atomic misfit of 8.41% between matrix and particle, indicating the semi-coherent interface and a certain degree of resistance against the crack propagation. Based on the above observation and analysis, the W-Zr-Ti

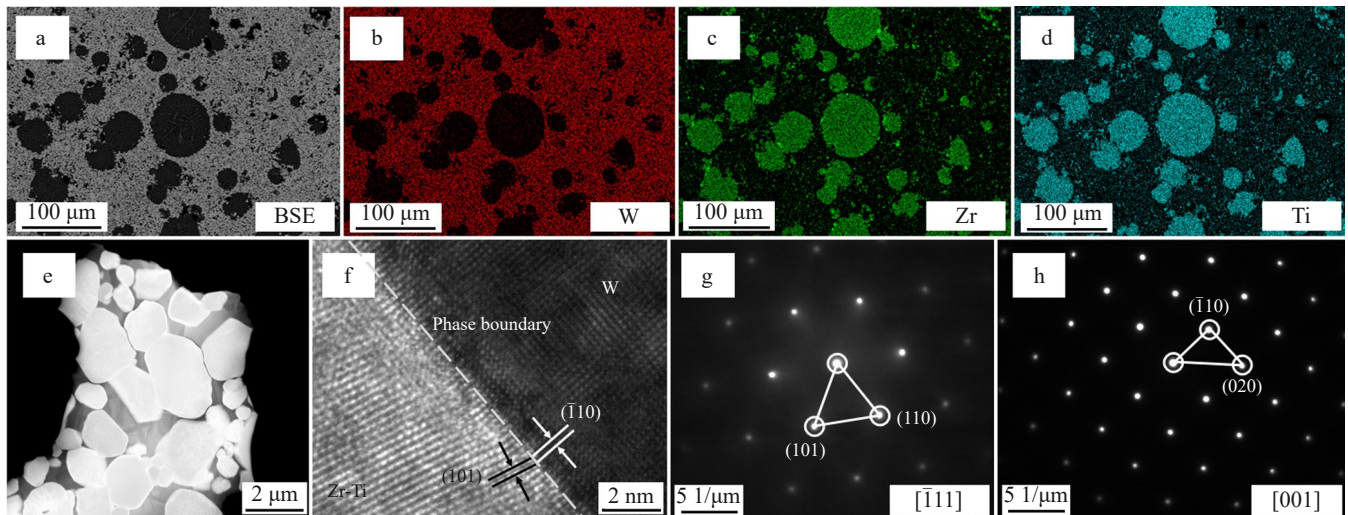


Fig.4 BSE image (a) and corresponding element mappings (b–d), HAADF-STEM image (e), HRTEM image (f) of W-Zr-Ti reactive alloy; SAED patterns of bonded matrix (g) and reinforced particle (h)

reactive alloy consists of Zr-Ti spheres (hcp), W particles (bcc), and Zr-Ti matrix (bcc). Meanwhile, it is supposed that the alloy has superior mechanical properties upon the compressive loading.

### 3.2 Chemical reaction and energetic characteristics

Dynamic loading by SHPB and heating loading by DSC/TG of the reactive alloy were conducted. Fig.5a shows high-speed camera images of chemical reaction during SHPB test. The results recorded by high-speed camera confirm that high-density W-Zr-Ti reactive alloy samples ignite and combust

under the condition of dynamic impact. On the contrary, there is no reaction phenomenon upon the quasi-static compression. After dynamic impact, the reactive alloy samples are crushed and form small-sized energetic debris. The debris flies at high velocities and disperses in the air. Because of the impact temperature rise by the plastic deformation and crack propagation<sup>[24]</sup>, chemical reaction is stimulated and bright sparks emerge. It is noting that the reaction intensity is influenced by the strain rate of impact loading. When the strain rate increases, the debris size decreases, the temperature

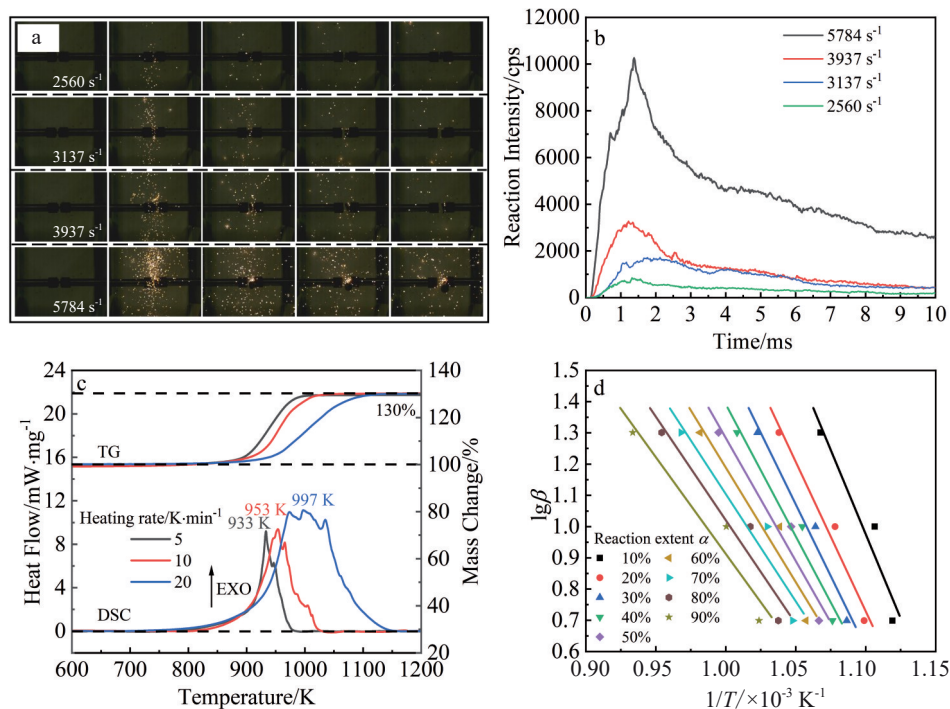


Fig.5 Chemical reaction and energetic characteristics of reactive alloy: (a) high-speed camera images of chemical reaction during SHPB test at different strain rates, (b) temporal distribution of reaction intensity at different strain rates represented by spark pixels, (c) DSC/TG thermal analysis results at different heating rates, and (d) fitting curves of FWO approach in various reaction extents

rises, and the specific surface area of the reactive alloy sample increases, leading to more violent combustion and stronger energy release phenomenon.

Digital image processing technique was utilized to analyze the combustion process intuitively, as shown in Fig. 5b. High-speed camera images can be divided into red, blue, and green matrices, and RGB images were transformed into binary images. Finally, the pixels of reaction sparks at different times were counted statistically. The curves of reaction intensity represented by the spark pixels could be divided into linear increasing period and exponential decreasing period. Reaction intensity rapidly rises and achieves the peak value in approximately 1.5 ms, and then comes into attenuation slowly. With the increase in strain rate, the peak value of the reaction intensive increases, while the attenuation of the curve becomes steeper, demonstrating that there are more consumption of energetic element and higher combustion efficiency at the higher strain rate.

Fig. 5c displays DSC/TG thermal analysis results of the reactive alloy at different heating rates. Reactive alloy samples exhibit an exothermic peak and mass increasing behavior during the heating loading. The average peak value is 961 K, corresponding to the energy release behavior of the alloy. DSC/TG curves of the samples begin to rise at the temperature of approximately 787 K. This initial temperature is higher than the ignition temperature of Zr (approximately 673 K)<sup>[30]</sup> and lower than the phase-transition temperature of Zr-Ti solid solution (approximately 883 K at equivalent atom ratio). One possible explanation is that the formation of Zr-Ti solid solution increases the temperature threshold, because Ti possesses higher ignition temperature than Zr<sup>[30]</sup>. Moreover, the addition of abundant W particles might reduce the oxygen quantity of diffusion effect into the reactive alloy per unit time compared with the pure Ti or Zr, because the W particles may embed into the interface between alloy and air, resulting in the delay of chemical reaction. The experimental result shows that the mass percent increases to approximately 130%, which is higher than 115% (element W remains inert, Zr and Ti perform reactive) and lower than 134% (elements W, Zr, and Ti perform reactive). It is considered that not only the elements Zr and Ti but also element W participate in the oxidation reactions. One possible explanation is that the W particles in this investigation are small enough, accompanied by the violent reaction of Zr and Ti, they are likely to react as well<sup>[21]</sup>. Combined with the analysis of Zr-Ti phase diagram, the exothermic peak ranged from 773 K to 1173 K may be interpreted as the phase transformation and combustion of Zr-Ti solid solution. It is inferred that  $\alpha$ -Zr (Ti) to  $\beta$ -Zr (Ti) and Zr (Ti) to ZrO<sub>2</sub> (TiO<sub>2</sub>) may be the main chemical reactions in loading condition. Additionally, element W may also transform into WO<sub>3</sub> in this process. Physically, there are challenges for the energetic characteristic investigation of the reactive alloy. In particular, it is difficult to clarify the reaction product under various circumstances. Further exploration may provide more evidence and better understanding in the reaction mechanism of the reactive alloy.

Additionally, pre-exponential factor and activation energy in Arrhenius equation were determined by Kissinger, Flynn-Wall-Ozawa (FWO), and Sateva-Sestak approach. Kissinger approach can be expressed by the following equation<sup>[31]</sup>.

$$\ln \frac{\beta}{T_p} = \ln \frac{A_k R}{E_k} - \frac{E_k}{RT_p} \quad (4)$$

where  $\beta$  refers to the heating rate,  $T_p$  corresponds to the peak temperature,  $R$  represents universal gas constant (8.3145 J·mol<sup>-1</sup>·K<sup>-1</sup>),  $A_k$  and  $E_k$  are pre-exponential factor and activation energy fitted by Kissinger approach, respectively.

As a complement of the calculation, FWO approach was employed to reduce errors caused by the assumption of reaction type function. Herein, activation energy at various reaction extents were fitted by Eq. (5), and the reaction extents were obtained by TG curves and calculated by Eq. (6):

$$\lg \beta = \lg \frac{A_f E_f}{RG(\alpha)} - 2.315 - 0.4567 \frac{E_f}{RT_i} \quad (5)$$

$$\alpha = \frac{w_i - w_b}{w_e - w_b} \quad (6)$$

where  $\alpha$  refers to reaction extent calculated by the mass percents;  $w_b$  and  $w_e$  donate the mass percents in the beginning and end of TG curves, respectively;  $w_i$  stands for the mass percent taken into account at the interest reaction extent;  $T_i$  refers to the temperature corresponding to the interest reaction extent;  $G(\alpha)$  represents the reaction type function. However, there is no requirement for specific formula of this function in FWO approach.  $A_f$  and  $E_f$  are pre-exponential factor and activation energy fitted by FWO approach, respectively.

To further reveal the reaction kinetics characteristic of reactive alloy, Sateva-Sestak approach was used in this investigation, which is suitable for solid reaction under non-isothermal condition. Relationship between the reaction type function and corresponding temperature can be written as the following equation.

$$\lg G(\alpha) = \lg \frac{A_s E_s}{R\beta} - 2.315 - 0.4567 \frac{E_s}{RT_i} \quad (7)$$

where  $A_s$  and  $E_s$  are pre-exponential factor and activation energy fitted by Sateva-Sestak approach, respectively. The other parameters are the same as the above approaches. Notably, the specific formula of reaction type function is essential in this approach. In particular, a reliable result needs to be verified by the following criterion as shown in Eq. (8–10), demonstrating that the selection of reaction type function is appropriate.

$$0 < E_s < 400 \text{ kJ} \cdot \text{mol}^{-1} \quad (8)$$

$$\left| \frac{E_f - E_s}{E_f} \right| \leq 0.1 \quad (9)$$

$$\left| \frac{\lg A_s - \lg A_k}{\lg A_k} \right| \leq 0.2 \quad (10)$$

The reaction kinetics parameters have been obtained using the above approaches. Kissinger approach result demonstrates that activation energy and pre-exponential factor are approximately 145.07 kJ·mol<sup>-1</sup> and 1.47×10<sup>7</sup> s<sup>-1</sup>, respectively, with a goodness of fit  $R^2=0.9527$ . Fitting curves and results obtained by FWO approach are illustrated in Fig. 5d and Table 1. It is

**Table 1 Fitting results of FWO approach for reactive alloy**

Reaction extent, $a/\%$	Temperature at 5 K/min, $T_{5K}/K$	Temperature at 10 K/min, $T_{10K}/K$	Temperature at 20 K/min, $T_{20K}/K$	Activation energy, $E_k/kJ\cdot mol^{-1}$	Goodness of fit, $R^2$
10	893.6	903.8	936.6	196.29	0.9203
20	910.0	927.6	963.4	174.10	0.9677
30	920.4	939.8	977.8	166.89	0.9713
40	929.2	948.2	992.0	153.91	0.9568
50	937.6	955.4	1005.2	143.25	0.9376
60	945.8	963.0	1018.8	133.43	0.9224
70	954.4	971.2	1033.0	125.03	0.9096
80	963.8	982.8	1048.0	120.62	0.9175
90	976.8	999.6	1071.2	112.71	0.9279

found that activation energy has a decreasing trend with the increase in reaction extent, which decreases from 196.29  $kJ\cdot mol^{-1}$  to 112.71  $kJ\cdot mol^{-1}$  when the reaction extent increases from 10% to 90%. The average of activation energy is 144.50  $kJ\cdot mol^{-1}$ , demonstrating a good consistency with Kissinger approach calculation. Furthermore, Sateva-Sestak approach supports that an Avrami-Erofeev  $n$ -dimensional nucleation/growth model with  $n=0.27$  might control the exothermic reaction of the reactive alloy. The average values of activation energy and pre-exponential factor are 142.40  $kJ\cdot mol^{-1}$  and  $2.19\times 10^7 s^{-1}$ , respectively.

### 3.3 Enhanced damage effect under explosion loading

Fig. 6 shows the experiment scene after reactive fragment explosion. It is demonstrated that reactive fragment made of high-density W-Zr-Ti alloy perforated the steel target and the shell of fuel tank successfully. When the reactive fragment penetrated the back shell of fuel tank, burning energetic debris and gas-liquid mixture sprayed in the air, causing violent combustion flame. Therefore, the reactive fragments possess sufficient mechanical strength to protect their damage potential during the explosion loading, and finally perforate the target as well as enhance the damage effect combined with kinetic penetration and chemical energy.

Based on the one-dimensional shock wave theory, shock pressure and energy of the reactive fragment in this experiment could be estimated<sup>[25]</sup>. By introducing the interface continuity condition, fragment and target have the same shock



Fig.6 Experiment scene after structure explosion

pressure and the vector sum of their material particles equals to the fragment velocity before collision.

$$P_1 = P_2 \quad (11)$$

$$v = u_{p1} + u_{p2} \quad (12)$$

where  $P_1$  and  $P_2$  are the shock pressure values of fragment and target, respectively;  $v$  refers to fragment velocity before collision;  $u_{p1}$  and  $u_{p2}$  represent the material particle velocities of fragment and target, respectively.

For the fragment and target, shock pressure values are expressed as follows:

$$P_1 = \rho_{01} u_{s1} u_{p1} \quad (13)$$

$$P_2 = \rho_{02} u_{s2} u_{p2} \quad (14)$$

where  $\rho_{01}$  and  $\rho_{02}$  are the densities of the fragment and target, respectively;  $u_{s1}$  and  $u_{s2}$  refer to the velocities of shock waves in the fragment and target, respectively.

Relationship between the velocities of shock waves and material particles are as follows:

$$u_{s1} = c_1 + s_1 u_{p1} \quad (15)$$

$$u_{s2} = c_2 + s_2 u_{p2} \quad (16)$$

Hugoniot parameters ( $c_1$ ,  $c_2$ ,  $s_1$ , and  $s_2$ ) are calculated using mixture law of the materials<sup>[32]</sup>.

According to the above equations, material particle velocity in the fragment is calculated by Eq.(17–18).

$$u_{p1} = v - \frac{(\rho_{01} c_1 + \rho_{02} c_2 + 2\rho_{01} s_1 v) - \Delta^{\frac{1}{2}}}{2(\rho_{02} s_2 - \rho_{01} s_1)} \quad (17)$$

$$\Delta = (\rho_{01} c_1 + \rho_{02} c_2 + 2\rho_{01} s_1 v)^2 - 4\rho_{01}(\rho_{02} s_2 - \rho_{01} s_1)(c_1 v + s_1 v^2) \quad (18)$$

Shock energy in the fragment is relevant to the shock pressure, material particle velocity, and loading time, calculated by Eq.(19–20).

$$E_p = P_1 u_{p1} \tau \quad (19)$$

$$\tau = \min \left\{ \frac{2h_1}{u_{s1}}, \frac{2h_2}{u_{s2}} \right\} \quad (20)$$

where  $E_p$  refers to shock energy;  $\tau$  is the loading time of shock wave, which is related to wave propagation both in the fragment and target;  $h_1$  and  $h_2$  are the thicknesses of fragment and target, respectively.

Reactive fragment impacts the target with the average

velocity of 1465 m/s measured by the experimental apparatus.  $c_1$ ,  $c_2$ ,  $s_1$ , and  $s_2$  equal to 4139 m/s, 4569 m/s, 1.197, and 1.490, respectively. Thicknesses  $h_1$  and  $h_2$  equal to 6.5 mm and 6.0 mm, respectively. And densities  $\rho_{01}$  and  $\rho_{02}$  equal to 10.43 g/cm<sup>3</sup> and 7.86 g/cm<sup>3</sup>, respectively. Hence, shock pressure of 35.77 GPa and shock energy of  $5.18 \times 10^4$  kJ/m<sup>2</sup> are acquired by calculation. Based on the above analysis and the violent combustion phenomenon, the actual reaction threshold must be lower than the computation, and the extraordinary damage effect of this new kind of W-Zr-Ti reactive alloy demonstrates its availability for engineering applications.

### 3.4 Quasi-static and dynamic behavior

Fig. 7a and 7b show the stress-strain curves of the reactive alloy under quasi-static and dynamic compression, respectively. Under quasi-static compression, the average compressive strength and fracture strain are 1.33 GPa and 0.118, respectively. High level of consistency and repeatability of the stress-strain curves indicate the experimental reliability, as shown in Fig. 7a. It is found that a brief yield platform appears before the fracture. This phenomenon may be attributed to the combination of brittle and ductile fracture resulted from the microstructure of the reactive alloy. Further evidence will be provided by the fracture morphology of experimental samples. However, high yield strength and compressive strength performance come to light in this alloy. It is supposed that fine W reinforced particles surrounding the Zr-Ti spheres and partial Zr-Ti matrix block the movement of distortion and generate Orowan stress reinforcement, leading to the improvement of yield strength<sup>[33]</sup>. Moreover, high compressive strength is probably caused by the force chain enhancement of W particles. As shown in Fig. 7b, reactive alloy presents strain

rate hardening effect under dynamic loading. With the increase in strain rate from 2560 s<sup>-1</sup> to 5784 s<sup>-1</sup>, compressive strength increases from 1.87 GPa to 2.25 GPa, and fracture strain decreases from 0.062 to 0.036. Besides, there is no obvious yield platform during dynamic compression, indicating the promotion of alloy brittleness at high strain rate. This phenomenon might be attributed to the loss of force chain stability and rapid crack propagation.

Based on the above experimental data, the constitutive model of reactive alloy was established. Although Johnson-Cook and Zerilli-Armstrong constitutive models have been employed to describe elastic-brittle reactive materials such as W-Zr alloy, poor consistency was obtained in the previous work<sup>[34]</sup>. Thus, one-dimensional elastic-brittle constitutive model with damage coefficient<sup>[35]</sup> was conducted in this study. Relationship between stress ( $\sigma$ ) and strain ( $\epsilon$ ) in this model is expressed as Eq. (21):

$$\sigma = E(1 - D)\epsilon \tag{21}$$

where  $E$  means the elastic modulus of the material. Damage coefficient  $D$  ranging from 0 to 1 is brought into the equation to demonstrate the influence of crack propagation and damage evaluation on the elastic modulus.

$$D = m\epsilon^{n_c} \tag{22}$$

where  $m$  and  $n_c$  represent parameters characterizing the variation of damage coefficient  $D$  with true strain.

Hence, one-dimensional elastic-brittle constitutive model can be expressed as follows:

$$\sigma = E\epsilon(1 - m\epsilon^{n_c}) \tag{23}$$

It is found that quadratic functions give satisfactory results in the fitting process of  $E$ ,  $m$ , and strain rate  $\dot{\epsilon}$ , as seen in

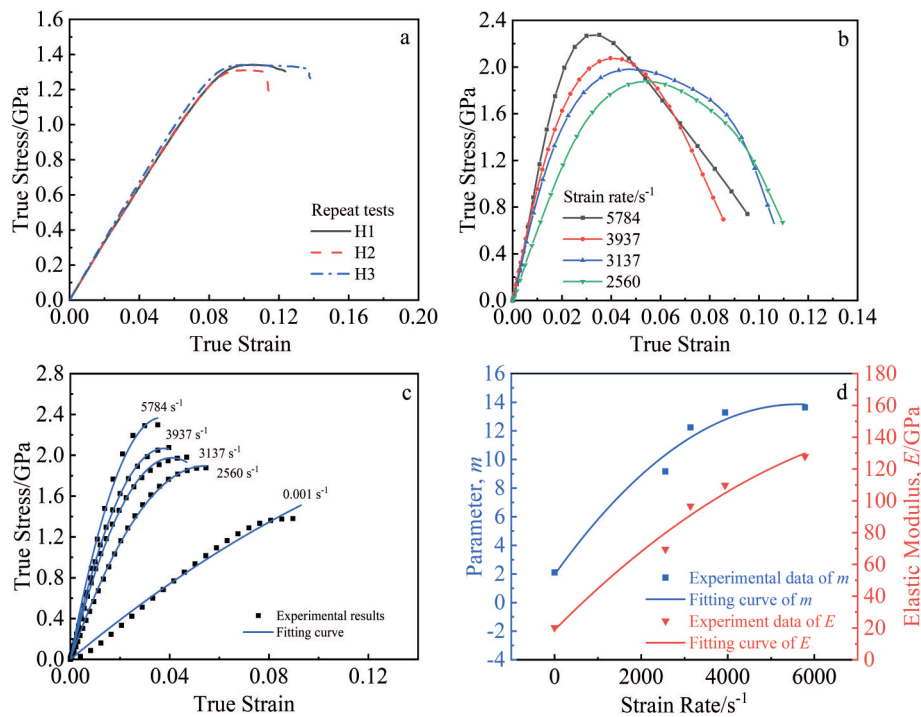


Fig. 7 True stress-true strain curves of reactive alloy under quasi-static compression (a) and dynamic impact (b); fitting curves of one-dimensional elastic-brittle constitutive model (c), parameter  $m$  and elastic modulus  $E$  (d)

Eq.(24–25). In present work,  $n_c=1$  is suitable for this kind of material, leading to a second-order Taylor expansion accuracy.

$$E = A_1 + A_2\dot{\epsilon} + A_3\dot{\epsilon}^2 \quad (24)$$

$$m = B_1 + B_2\dot{\epsilon} + B_3\dot{\epsilon}^2 \quad (25)$$

where  $A$  and  $B$  with subscripts 1–3 are the fitting parameters of  $E$  and  $m$ .

Table 2 and Fig.7c–7d show the fitting results and curves of the one-dimensional elastic-brittle constitutive model. The values of goodness of fit ( $R^2$ ) suggest that the fitting formulation are in good consistency with test data. Accordingly, the fitting curves correspond to the experimental results at different strain rates, as shown in Fig.7c. Elastic modulus  $E$  and parameter  $m$  increase with the increase in strain rate, and the increasing trends become slow gradually. Apparently,  $E$  and  $m$  exhibit a positive strain-rate sensibility, and increase by 6.33 and 6.47 times with strain rate ranging from  $0.001 \text{ s}^{-1}$  to  $5784 \text{ s}^{-1}$ , respectively. This result suggests the variation of force condition and damage evolution when the reactive alloy was subjected to dynamic loading. However, the fitting results of  $E$  and  $m$  versus strain rate were acquired using the least square method, as illustrated in Fig. 7d. The

**Table 2 Fitting results of constitutive model**

Number	Strain rate, $\dot{\epsilon}/\text{s}^{-1}$	Elastic modulus, $E/\text{GPa}$	$m$	Goodness of fit, $R^2$
1	0.001	20.22	2.1062	0.9871
2	2560	69.54	9.1685	0.9989
3	3137	96.69	12.2408	0.9991
4	3937	109.78	13.2784	0.9998
5	5784	127.91	13.6357	0.9939

values of  $R^2$  in the fitting of  $E$  and  $m$  are 0.9520 and 0.9532, respectively. Eventually, the constitutive formulation was obtained and well-fitted for further research, as shown in Eq. (26). As a consequence, one-dimensional elastic-brittle constitutive model is available to describe the dynamic behavior of high-density W-Zr-Ti reactive alloy, which presents favorable validity and accuracy.

$$\begin{cases} \sigma = E\epsilon(1 - m\epsilon) \\ E = 18.769 + 2.747 \times 10^{-2}\dot{\epsilon} - 10427 \times 10^{-6}\dot{\epsilon}^2 \\ m = 1.948 + 4.230 \times 10^{-3}\dot{\epsilon} - 3.764 \times 10^{-7}\dot{\epsilon}^2 \end{cases} \quad (26)$$

### 3.5 Fracture morphology and failure mechanism

Fig.8 shows fracture morphology of the reactive alloy. By analyzing the size and density of the phases illustrated in the BSE images of Fig.4 and Fig.8, the corresponding relationship between fracture morphology and alloy phase can be clarified. Under quasi-static compression, fine and distinct equiaxial dimples emerge on the fracture surface of Zr-Ti spheres as shown in Fig.8a, indicating the tensile failure characteristics. Interestingly, Zr-Ti matrix adhered on the W particles performs flowing and drawing manifestation, as shown in Fig.8b, resulting in the plastic deformation. At the strain rate of  $3137 \text{ s}^{-1}$ , incline and regular shear dimples appear on the fracture surface of Zr-Ti spheres as shown in Fig.8c, implying the increase in shear failure characteristics. Meanwhile, W particles become angular and unambiguous, as shown in Fig. 8d, demonstrating that the intergranular fracture occurs between W particles and Zr-Ti matrix. It is reasonable to hold the viewpoint that the brittleness of reactive alloy increases with the increase in strain rate, since identical results have been obtained by SHPB test and SEM observation. At the strain rate of  $5784 \text{ s}^{-1}$ , Zr-Ti spheres vanish and leave residual voids as shown in Fig.8e. The explanation of this phenomenon

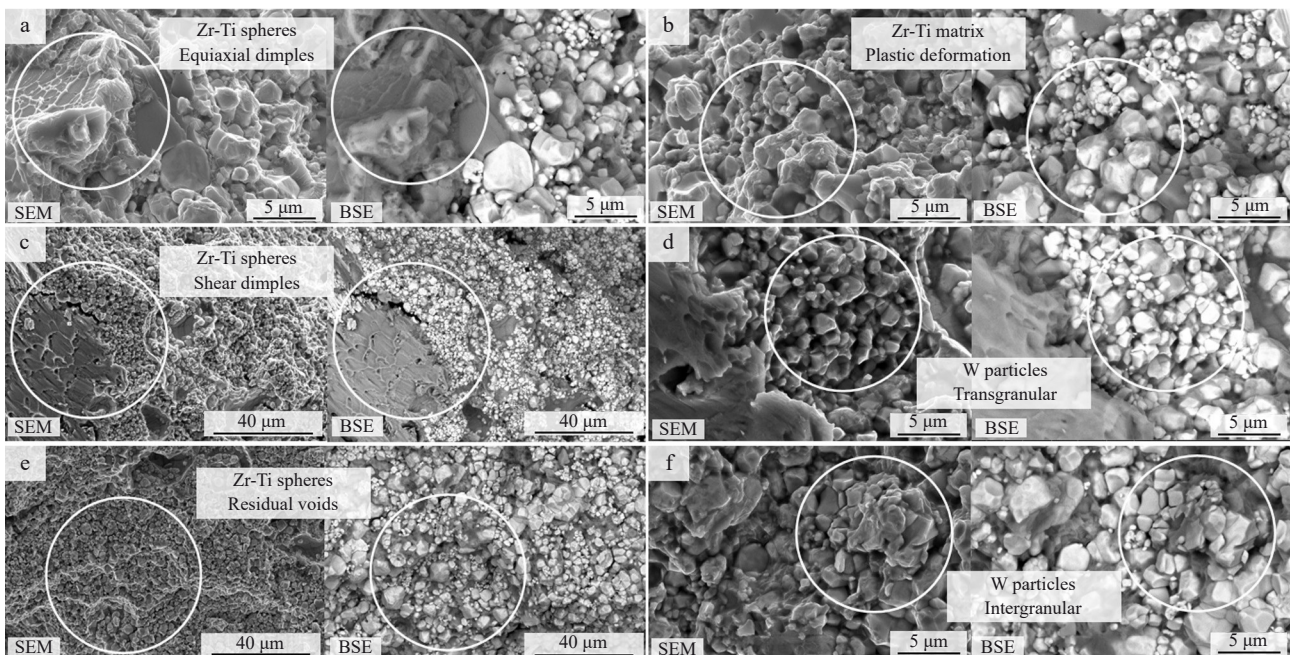


Fig.8 Fracture morphologies of reactive alloy at different states: (a–b) quasi-static compression at  $0.001 \text{ s}^{-1}$  strain rate; (c–d) dynamic impact at  $3137 \text{ s}^{-1}$  strain rate; (e–f) dynamic impact at  $5784 \text{ s}^{-1}$  strain rate

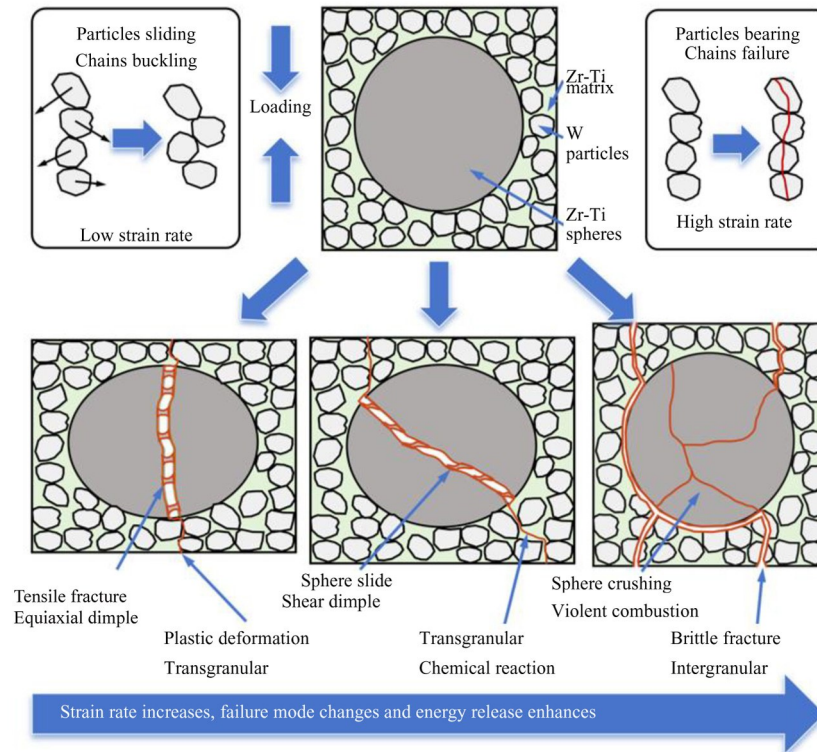


Fig.9 Schematic diagram of failure mechanism of reactive alloy

is that Zr-Ti spheres are crushed and react in the air at high strain rate. This result indicates that energy release enhances with the increase in strain rate, which can be verified by Fig. 5a. Notably, W particles begin to crush and perform transgranular combined with intergranular fracture behavior on this occasion as shown in Fig.8f. It is supposed that high strength and brittleness of the reactive alloy under high strain rate loading may be attributed to the bearing and crushing of W particles. As mentioned above, the transformation of fracture morphology has influence on dynamic behavior and energetic characteristics of the reactive alloy.

Fig.9 depicts schematic diagram of the failure mechanism of reactive alloy. Zr-Ti sphere (gray) is surrounded by W particles (white) and Zr-Ti matrix (green) for abstraction. During the loading process, three types of contact interfaces associated with W particles exist, including W particles to Zr-Ti spheres, W particles to Zr-Ti matrix, and between W particles. Among them, contact interface between W particles is likely to maintain strong bearing capacity, as well as lead to the formation of force chains. At low strain rate, W particles have enough time to slide and move in the Zr-Ti matrix, leading to the force chains buckling and plastic deformation of the alloy, because the stress loading on W particles are restricted and gradual. With the increase in strain rate, less movement of W particles and more chemical reaction of Zr-Ti matrix occur during the failure process. Meanwhile, stress concentration and unstable sliding emerge in the Zr-Ti spheres, resulting in the transformation from tensile dimples into shear dimples. At high strain rate, Zr-Ti spheres are entirely crushed and combust violently. Particularly, W

particles bear high level stress rapidly, which may exceed the ultimate strength of W, resulting in the failure of force chains. Therefore, reactive alloy performs intergranular fracture behavior in this case. The increase in strain rate leads to the variation of failure modes and contributes to the increase in compression strength and reaction intensity.

#### 4 Conclusions

1) High-density W-Zr-Ti reactive alloy prepared by powder metallurgy consists of Zr-Ti spheres (hcp), W particles (bcc), and Zr-Ti matrix (bcc). Semi-coherent interfaces exist between Zr-Ti matrix and W particles.

2) The reactive alloy performs high compression strength of 2.25 GPa at  $5784 \text{ s}^{-1}$  strain rate, and presents strain rate hardening effect under dynamic impact. SHPB test and DSC/TG thermal analysis demonstrate energy release behavior of the alloy during impact or heating at approximately 961 K.

3) Enhanced damage effect emerges in the explosion test, due to the penetration capability and violent combustion of the reactive fragments. It is found that reactive fragment is available for igniting fuel tank targets, and the shock pressure and energy thresholds are less than 35.77 GPa and  $5.18 \times 10^4 \text{ kJ/m}^2$ , respectively.

4) Dimples on the fracture surface are transformed into residual voids while intergranular fracture emerges with the increase in strain rate. During this transformation, force chains failure and spheres crushing play an important role in dynamic behavior and energetic characteristics.

## References

- 1 Zhang Y, Huang Y F, Liu W S et al. *Journal of Alloys and Compounds*[J], 2022, 891: 161881
- 2 Alaei M, Borhani G H, Bakhshi S R et al. *Materials Research Express*[J], 2019, 6(8): 0865h5
- 3 Ning J G, Ren H L, Guo T T et al. *International Journal of Impact Engineering*[J], 2013, 62: 60
- 4 Pedersen B, Bless S. *International Journal of Impact Engineering*[J], 2006, 33(1): 605
- 5 Wang Y, Huang Y F, Liu W S et al. *Journal of Alloys and Compounds*[J], 2023, 941: 168927
- 6 Zhao Kongxun, Liu Zeren, Zhang Zhouan et al. *Rare Metal Materials and Engineering*[J], 2023, 52(3): 999 (in Chinese)
- 7 Bauri R, Yadav D, Shyam C N et al. *Materials Science and Engineering A*[J], 2015, 620: 67
- 8 Mao R P, Xiang D P. *Materials and Design*[J], 2023, 225: 111468
- 9 Wu Z, Yang C M, Liu Q J et al. *Rare Metals*[J], 2014, 33(3): 330
- 10 Liu H X, Yang Y F, Cai Y F et al. *Rare Metals*[J], 2023, 42(8): 2713
- 11 Chen H H, Zhang X F, Liu C et al. *Acta Mechanica Sinica*[J], 2021, 37(6): 970
- 12 Chen H H, Zhang X F, Dai L H et al. *Defence Technology*[J], 2022, 18(8): 1470
- 13 Luo R M, Huang D W, Yang M C et al. *Materials Science and Engineering A*[J], 2016, 675: 262
- 14 Liu Zeren, Zhao Kongxun, Tang Yu et al. *Rare Metal Materials and Engineering*[J], 2023, 52(6): 2296 (in Chinese)
- 15 Liu X F, Tian Z L, Zhang X F et al. *Acta Materialia*[J], 2020, 186: 257
- 16 Hu X, Liu X, Yan D et al. *Journal of Alloys and Compounds*[J], 2022, 894: 162505
- 17 Zhou S, Jian R, Liang Y J et al. *Journal of Alloys and Compounds*[J], 2021, 859: 157796
- 18 Chen X W, Wei L M, Li J C. *International Journal of Impact Engineering*[J], 2015, 79: 102
- 19 Xu F Y, Yu Q B, Zheng Y F et al. *International Journal of Impact Engineering*[J], 2017, 104: 13
- 20 Wei H Y, Yoo C S. *Journal of Applied Physics*[J], 2012, 111(2): 023506
- 21 Coverdill A, Delaney C, Jennrich A et al. *Journal of Energetic Materials*[J], 2014, 32(3): 135
- 22 Zhang X F, Shi A S, Qiao L et al. *Journal of Applied Physics*[J], 2013, 113(8): 083508
- 23 Ren H L, Liu X J, Ning J G. *Materials Science and Engineering A*[J], 2016, 660: 205
- 24 Ren H L, Liu X J, Ning J G. *AIP Advances*[J], 2016, 6(11): 115205
- 25 Luo P G, Wang Z C, Jiang C L et al. *Materials and Design*[J], 2015, 84: 72
- 26 Liu H, Shi A H, Du X F et al. *International Journal of Impact Engineering*[J], 2023, 171: 104390
- 27 Wang L Y, Jiang J W, Li M et al. *Defence Technology*[J], 2021, 17(2): 467
- 28 Chen P, Guo L, Wang C T et al. *International Journal of Refractory Metals and Hard Materials*[J], 2023, 115: 106306
- 29 Xing L N, Liu X W, Cao Z M et al. *Materials Science and Engineering A*[J], 2022, 831: 142196
- 30 Xie Yanbo. *Study on the Influence of Ignition Threshold of Reactive Composite*[D]. Njing: Nanjing University of Science & Technology, 2021 (in Chinese)
- 31 Hu Rongzu, Shi Qizhen. *Thermal Analysis Kinetics*[M]. Beijing: Science Press, 2001 (in Chinese)
- 32 Xin Chunliang, Xue Zaiqing, Tu Jian et al. *Material Parameters Manual for Finite Element Analysis*[M]. Beijing: China Machine Press, 2022 (in Chinese)
- 33 Stefaniuk D, Kachanov M. *International Journal of Engineering Science*[J], 2023, 191: 103903
- 34 Ma Y, Wang C T, Guo Z P et al. *Journal of Applied Physics*[J], 2023, 134(17): 175103
- 35 Li Qiang, Jiang Chunlan, Wang Zaicheng. *Rare Metal Materials and Engineering*[J], 2015, 44(5): 1124 (in Chinese)

## 高密度 W-Zr-Ti 活性合金的动态力学行为、能量释放特性及断裂失效机制

祁宇轩<sup>1</sup>, 毛亮<sup>1</sup>, 李佩滢<sup>1</sup>, 刘桂涛<sup>2</sup>, 田龙年<sup>1</sup>, 姜春兰<sup>1</sup>

(1. 北京理工大学 爆炸科学与安全防护全国重点实验室, 北京 100081)

(2. 中国兵器科学研究院 宁波分院, 浙江 宁波 315103)

**摘要:** 利用粉末冶金工艺制备了一种高密度钨锆钛 (W-Zr-Ti) 活性合金, 其具有密度高、强度大和能量释放强的优点, 兼具优异的动能侵彻和反应释能效应。利用动态冲击试验发现该合金具有应变率强化效应, 并通过数字图像处理技术和热化学分析研究了其能量释放特性。结果表明, 在  $5784 \text{ s}^{-1}$  应变率下, W-Zr-Ti 活性合金的材料抗压强度高达 2.25 GPa, 其在 961 K 左右发生点火放热反应。基于爆炸测试及冲击波理论, 发现材料冲击压力和冲击能量阈值分别小于 35.77 GPa 和  $5.18 \times 10^4 \text{ kJ/m}^2$ 。此外, 揭示了材料断裂行为和失效模式的转变机制, 其导致了材料强度及反应程度在动态加载下的显著提高。

**关键词:** 活性合金; 动态力学行为; 能量释放特性; 断裂失效机制

作者简介: 祁宇轩, 男, 1999年生, 博士生, 北京理工大学爆炸科学与安全防护全国重点实验室, 北京 100081, E-mail: qi yuxuantj@163.com